Supplementary Material

Defects, Corrugation and Temperature Govern Rarefied-Air Drag on Graphene Coatings

Samuel Cajahuaringa,[1] Davide Bidoggia,[1] Maria Peressi,[1] and Antimo Marrazzo[2]
[1)] *Dipartimento di Fisica, Università di Trieste, I-34151 Trieste, Italy*
[2)] *Scuola Internazionale Superiore di Studi Avanzati (SISSA), I-34136 Trieste, Italy*

(Dated: 23 April 2026)

CONTENTS

S1. GRAPHENE-ALUMINA INTERFACE

Computational Setup and Interface Construction

All first-principles calculations are performed using the QUANTUM ESPRESSO distribution[1–3] and SSSP Precision v1.3 pseudopotentials[4–7]. First-principles structural optimizations are performed to establish reference geometries for the isolated components. Pristine graphene is optimized using the Perdew-Burke-Ernzerhof (PBE) functional[8] augmented with Grimme's D3 dispersion correction[9] (PBE+D3). A plane-wave kinetic energy cutoff of 50 Ry is applied to the wavefunctions, with a corresponding charge density cutoff of 450 Ry, and Brillouin zone integration employed a $12 \times 12 \times 1$ Monkhorst-Pack k-point grid. These calculations yield an optimized graphene lattice parameter of $a = 2.466$ Å. Bulk α-$Al_2O_3(0001)$ is optimized at the PBE level using again a plane-wave kinetic energy cutoff of 50 Ry for wavefunctions, with a charge density cutoff of 450 Ry and $12 \times 12 \times 5$ Monkhorst-Pack k-point grid, resulting in lattice constants of $a = 4.81$ Å and $c = 13.1454$ Å.

The α-$Al_2O_3(0001)$ slab is made of four layers, where the top and bottom aluminum layers are fully relaxed to obtain a surface structure consistent with established literature[10–15]. Calculations are performed with the PBE+D3 functional, a wavefunction cutoff of 50 Ry, a charge density cutoff of 450 Ry, and $12 \times 12 \times 5$ Monkhorst-Pack k-point grid.

To construct a commensurate graphene/α-$Al_2O_3(0001)$ interface while minimizing lattice mismatch, the graphene sheet is rotated by 26 degrees relative to the substrate. This rotation reduces the lattice mismatch to a negligible 0.04% of strain, enabling the construction of a common supercell matching the surface area of a (4×4) α-$Al_2O_3(0001)$ slab, resulting in a system of 422 atoms for the interface.

DFT absorption calculations

Interfacial binding properties are evaluated using the PBE+D3 functional with a plane-wave kinetic energy cutoff of 50 Ry for the wavefunction and 450 Ry for the charge density, a $3 \times 3 \times 1$ Monkhorst-Pack k-point grid and a vacuum buffer of 20 Å. The computed binding energy and equilibrium separation distance are in agreement with the values reported by D. Acharya et al.[12].

	$\Delta E_{abs}(eV/C)$	d_{abs} (Å)
This work	-0.050	3.08
Debito et al.[12]	-0.051	2.67-3.16

TABLE S1. $\Delta E_{abs}(eV/C)$ is the adsorption energy per carbon atom and d_{abs} is the adsorption distance between graphene and alumina surface.

Alt text: Table comparing adsorption energy per carbon atom and adsorption distance for graphene on alumina, as obtained in this work and by Debito et al.. The adsorption energy is approximately -0.05 eV per carbon atom in both cases. The adsorption distance is 3.08 Åin this work and ranges from 2.67 to 3.16 Åin the reference, showing good agreement between the results.

The relatively low magnitude of the adsorption, characteristic of physisorption, combined with the absence of significant charge transfer across the interface, confirms that the graphene–alumina interaction is predominantly governed by van der Waals forces.

Classical Force Field Parameterization

Given the non-covalent nature of the interface, a Lennard-Jones (LJ) pair potential is developed to describe the Al–C and O–C interactions. The LJ parameters are optimized by fitting the DFT adsorption energy curve using the differential evolution optimization method[16]. The population consists of 40 individuals and the space region is limited by 0.005—0.04 eV for ε_{Al-C}, 2.9—3.5 Å for σ_{Al-C}, 0.002—0.005 eV for ε_{O-C} and 2.0—3.1 Å for σ_{O-C}, with mutation factor 0.5 and cross rate 0.8. We use a custom cost function defined by a weighted mean absolute error (WMAE) between the LAMMPS-computed binding energies and the reference DFT energies across the interfacial separation profile:

$$WMAE = \frac{\sum_i w_i |E_i^{LJ} - E_i^{DFT}|}{\sum_i w_i} \tag{S1}$$

where the weighting factor is defined as $w_i = 1/(|E_i^{DFT} - E_{min}^{DFT}| + \delta)$, with $\delta = 10^{-6}$ eV introduced for numerical stability. This inverse-energy weighting scheme deliberately amplifies the contribution of data points near the potential energy minimum,

	$\varepsilon(eV)$	σ (Å)
Al-C	0.0112	3.242
O-C	0.0049	2.073

TABLE S2. LJ parameters optimized with DFT (PBE+D3) for graphene on α-$Al_2O_3(0001)$.

Alt text: The optimized Lennard-Jones parameters for the Al-C interaction are $\varepsilon = 0.0112$ eV and $\sigma = 3.242$ Å, while for the O-C interaction, $\varepsilon = 0.0049$ eV and $\sigma = 2.073$ Å.

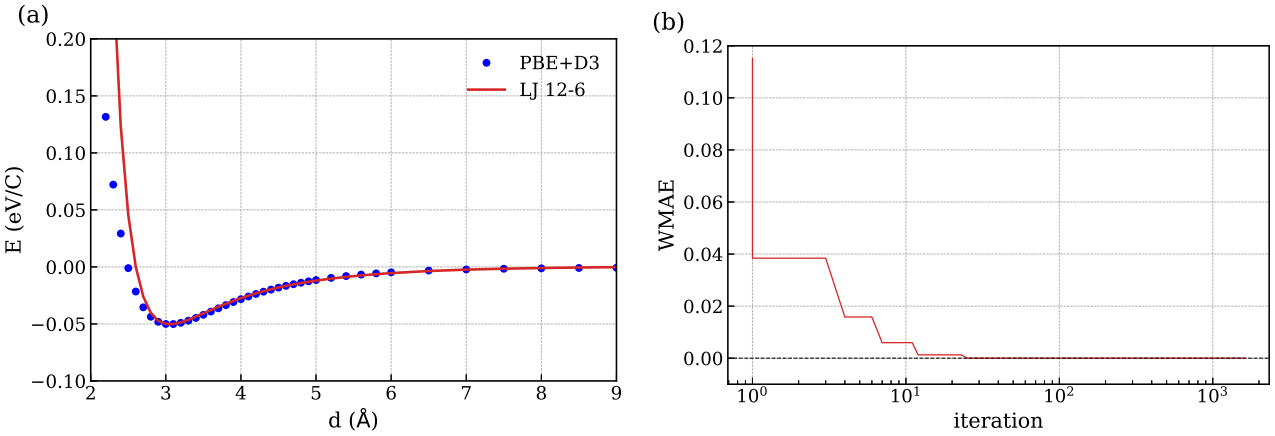

FIG. S1. (a) Adsorption energy profile computed with DFT and the corresponding optimized LJ force field. (b) WMAE evolution of best individual as function of numbers of iterations.

Alt text: Panel (a) shows the adsorption energy profile for graphene on alumina as a function of interfacial separation, comparing DFT results with the optimized Lennard-Jones potential. The two curves show good agreement, particularly near the energy minimum correctly reproducing the equilibrium binding distance and well depth. Panel (b) illustrates the convergence of the optimization process, with the weighted mean absolute error monotonicallydecreasing over iterations.

ensuring that the equilibrium binding distance and well depth are reproduced with high fidelity (see Fig. S1a). The optimized LJ parameters are reported in the Table S1.

The resulting fitted potential demonstrates well agreement with the reference DFT data. This validates the transferability of the derived force field for subsequent large-scale molecular dynamics simulations of graphene/α-alumina systems.

S2. COMPUTATIONAL DETAILS

Generation and thermalization of slabs.

To generate these slabs, we first compute the equilibrium lattice constants for the bulk crystals (with hexagonal symmetry) under an isothermal-isobaric (NPT) ensemble from room temperature until 900 K and 1 atm pressure for 100 ps to compute the thermal averages. Periodic boundary conditions are applied in all three spatial dimensions during the bulk equilibration phase. To build the graphene-coated α-$Al_2O_3(0001)$ structures, we follow the protocol displayed in Fig. S2. We select the alumina and graphene units cell relaxed at a given temperature (T_0), then for each temperature we build a common supercell (not necessarily hexagonal) which accomodates both alumina and graphene allowing for a small strain in the latter using the CellMatch code[17]. We try different relative orientation between the cells until a common supercell with a strain for graphene less than 0.0001 (area ratio) is obtained. Calculations for bare alumina α-$Al_2O_3(0001)$ surface are performed on the same structures by removing carbon atoms.

Before thermalization, the atomic coordinates of each surface are optimized via energy minimization to eliminate any residual strain or unphysical forces. Following minimization, the surfaces are equilibrated in the canonical (NVT) ensemble for 100 ps to ensure thermal stability before introducing gas molecules.

We use the graphene-coated α-$Al_2O_3(0001)$ surface structure at room temperature to create the interfaces with different concentration of defects; except for the lowest concentration of defects (0.14%), where we considered a $2 \times 2 \times 1$ supercell.

T (K)	$a_{Al_2O_3}$ (Å)	a_{Gr} (Å)
298	4.7912	2.4168
400	4.7997	2.4164
500	4.8082	2.4162
600	4.8171	2.4161
677	4.8237	2.4161
700	4.8258	2.4161
800	4.8353	2.4161
900	4.8447	2.4162

TABLE S3. Lattice parameters for alumina and graphene as a function of temperature, modeled by Vashishta[18] and AIREBO[19] potentials, respectively.

Alt text: Table listing the lattice parameters for alumina and graphene at various temperatures. The lattice parameter for alumina increases from 4.7912 Å at 298 K to 4.8447 Å at 900 K, while the lattice parameter for graphene remains nearly constant around 2.416 Å across the temperature range.

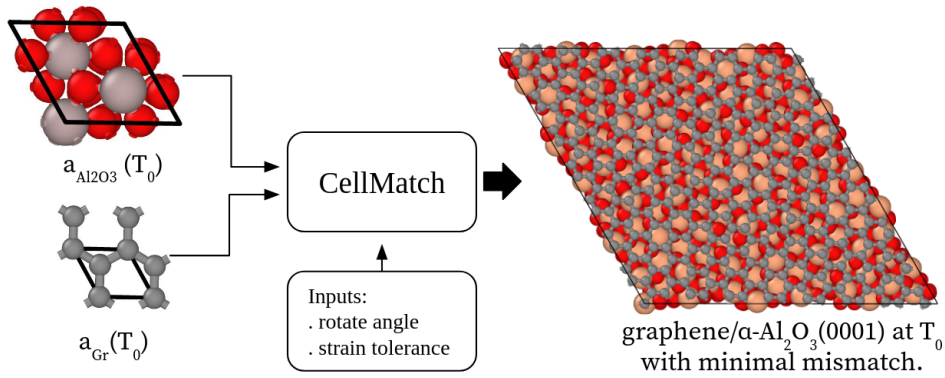

FIG. S2. Workflow to build the relaxed graphene-coated alumina surface at different temperatures.

Alt text: Schematic workflow for constructing the relaxed graphene-coated alumina surface. The process consistes in the optimiztion of both alumina and graphene structures at a given temperature, then the construction of a common supercell with minimal strain utilizing the CellMatch code.

Task farming

The large-scale computation of scattering trajectories constitutes a heterogeneous workload because trajectories are sampled over a wide range of initial conditions, leading to variable run times across tasks. This type of *embarrassingly parallel* workload is commonly referred to as *task farming*. We therefore employ HyperQueue[20], a meta-scheduler for task farming that operates on top of high-performance computing (HPC) workload managers. HyperQueue groups many fine-grained tasks into a smaller number of scheduler allocations and then dynamically load-balances tasks across allocated nodes and cores.

S3. MONTE CARLO SAMPLING OF MOLECULAR-BEAM SCATTERING

In order to mimic traditional molecular gas beam experiments, where a collimated beam of N_2 molecules is directed toward the surface at fixed incidence angles and velocities, each trajectory is initialized with a prescribed speed (sampled from a narrow distribution centered on the experimental beam velocity) and a defined incident polar angle θ_i, while the lateral position and azimuthal orientation are randomized over the surface. Fig. S3a illustrates the scattering trajectory of a nitrogen molecule on a graphite surface. The initial conditions of a linear molecule such as N_2 are specified by the following variables:

$$\mathbf{r}_i = (x_i, y_i, r_c; \theta_r, \phi_r), \tag{S2}$$

$$\mathbf{v}_i = (-v\sin\theta_i\cos\phi, -v\sin\theta_i\sin\phi, -v\cos\theta_i) \tag{S3}$$

$$\omega_i = (\omega, \psi) \tag{S4}$$

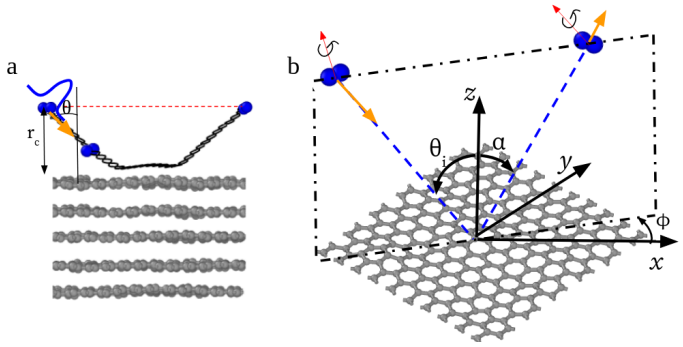

FIG. S3. Gas beam scattering at fixed incoming angle: (a) example of scattering trajectory, (b) Incident and reflected velocities.

Alt text: Panel (a) illustrates a scattering trajectory of a nitrogen molecule on a graphite surface. θ angle is here defined as the incident angle. Panel (b) shows the incident and reflected velocity vectors, defining α as the reflected angle and ϕ as the azimuthal angle. Conventionally the z axis is taken to be normal to the surface.

where $\mathbf{r}_i$ describes the position of the center of the molecule, while θ_r and ϕ_r represent its orientation. $\mathbf{v}_i$ is the velocity of center and ω_i its angular velocity. The gas molecules are launched from a fixed height above the surface, $z = r_c$. Their lateral position and molecular orientation are randomized across the surface, and can be sampled as

$$x_i = L_x \xi_1, \tag{S5}$$
$$y_i = L_y \xi_2, \tag{S6}$$
$$\phi_r = 2\pi\xi_3, \tag{S7}$$
$$\theta_r = \sin^{-1}(2\xi_4 - 1) + \frac{\pi}{2}. \tag{S8}$$

where L_x and L_y are determined by the lateral dimensions of the surface, and $\xi_1, \xi_2, \xi_3, \xi_4$ are random variables uniformly distributed on the interval $[0,1]$. The incident (translational and rotational) velocities are set at a fixed incidence angle θ_i, with a random azimuthal orientation given by $\phi = 2\pi\xi_5$.

Gas beam scattering experiments on graphite were carried out under the following conditions: a supersonic N_2 beam was formed by expanding the gas through a pinhole nozzle of 125 μm diameter. The nozzle was held at 296 K, yielding N_2 molecules with a nominal velocity of $v = 1453$ m/s and a velocity width (full width at half maximum, FWHM) of $\Delta v = 151$ m/s[21].

A supersonic molecular beam is not simply a thermal gas at equilibrium (as described by the Maxwell-Boltzmann distribution), but rather a beam produced by the expansion of a gas through a nozzle. When a gas expands from high pressure through a nozzle into vacuum, a substantial fraction of its random thermal energy is converted into directed (streaming) motion along the beam axis. The molecules are accelerated because the high-pressure gas upstream of the nozzle drives the flow, while collisions within the expansion region redistribute thermal motion into coherent bulk velocity. This process can be approximated as an adiabatic expansion, leading to a terminal beam speed of

$$v \approx \sqrt{\frac{2\gamma}{\gamma - 1}\frac{k_B T_0}{m}} = 1450 \quad m/s \tag{S9}$$

where $T_0 = 296$ K is the nozzle temperature, $m = 14.007$ amu is the N_2 mass and γ the adiabatic coefficient, that is equal to 7/5 for diatomic molecules. In a nozzle expansion, most translational thermal motion is converted into directed flow, but rotational degrees of freedom still in thermal equilibrium and described by the Maxwell-Boltzmann distribution. The velocities (translational and rotational) are sampled by:

$$v \Leftarrow \mathcal{N}(v, \sigma = \Delta v/(8\ln 2)) \tag{S10}$$
$$\phi = 2\pi\xi_6 \tag{S11}$$
$$\omega \Leftarrow \frac{I}{K_B T_0}\omega e^{-\frac{I\omega^2}{2K_B T_0}} \tag{S12}$$

where I is the moment of inertia of the molecule, ω is the magnitude of its angular velocity, and ψ denotes the ratio of the angular-velocity components in the molecular frame[22].

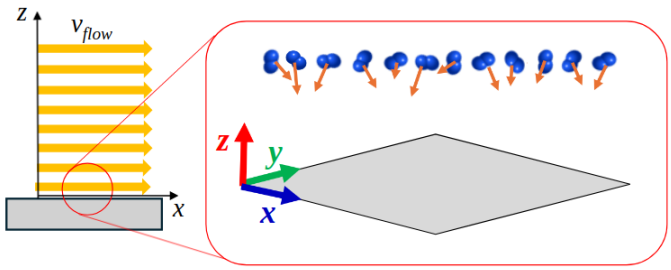

FIG. S4. Schematic representation of a rarefied gas flow interacting with a surface; at the microscopic level, the gas is assumed to be in thermal equilibrium with a drift velocity tangential to the surface.

Alt text: The gas flow is oriented along the x axis direction, parallel to the surface, while the thermal velocity distribution of the gas molecules is represented by a Maxwell-Boltzmann distribution centered around this non-zero drift velocity.

S4. MONTE CARLO SAMPLING OF RAREFIED GAS-FLOW SCATTERING

In order to study drag induced by a gas flow (Fig. S4) under highly rarefied conditions, it is necessary to sample the full range of molecular initial velocities, rather than restricting the dynamics to a fixed incidence angle and a narrowly distributed beam speed. This can be achieved by drawing translational and rotational velocities from the equilibrium distributions at a prescribed temperature. The numerical setup is otherwise analogous to that described in the previous section. The initial molecular position and orientation are sampled using Eq. (S2); in the present case, the translational and rotational velocities are drawn from the corresponding Maxwell-Boltzmann distributions, given by

$$v_x \Leftarrow \sqrt{\frac{m}{2\pi K_B T}} e^{-\frac{m}{2K_B T}(v_x - v_{flow})^2}, \tag{S13}$$

$$v_y \Leftarrow \sqrt{\frac{m}{2\pi K_B T}} e^{-\frac{m}{2K_B T} v_y^2}, \tag{S14}$$

$$v_z \Leftarrow \frac{m}{K_B T} v_z e^{-\frac{m}{2K_B T} v_z^2} \quad v_z < 0, \tag{S15}$$

$$\phi = 2\pi\xi_7 \tag{S16}$$

$$\omega \Leftarrow \frac{I}{K_B T_0} \omega e^{-\frac{I\omega^2}{2K_B T_0}}, \tag{S17}$$

In this case, v_x denotes the molecular velocity component along the flow direction, v_y is the tangential component perpendicular to the flow, and v_z is the normal component, which by convention is taken to be positive when pointing away from the surface. The rotational velocities are described following the same convention as in the previous section.

S5. COLLISION STATISTICS FOR SCATTERING TRAJECTORIES

Fig. S5 summarizes the collision statistics for the three surfaces considered: graphite, α-$Al_2O_3(0001)$, and graphene-coated α-$Al_2O_3(0001)$. Bars shown in bold colors correspond to single-collision events, whereas lighter shades indicate trajectories undergoing multiple collisions before escaping from the surface. In our gas-beam simulations, all molecules are ultimately reflected and we do not observe nitrogen trapping on any surface. This is ensured by employing a sufficiently long maximum simulation time (100 ps), which minimises the risk of misclassifying slowly desorbing trajectories and thereby improves the accuracy of the extracted angular distributions.

Fig. S6 is the angular scattering distribution for the three surfaces considered in this study.

S6. ACCOMMODATION COEFFICIENTS

To compute the accommodation coefficients (ACs), we first collect collision data from the MD simulations and then analyse the correlations between the relevant incoming and outgoing velocity components[23]. These correlations can be represented as two-dimensional probability-density maps: for a given set of incident translational and rotational velocities, they provide the

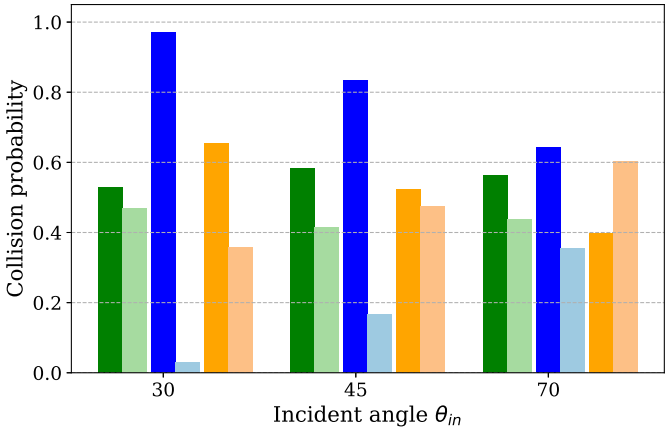

FIG. S5. Collision statistics for N_2 scattering-trajectory simulations on (i) a multilayer graphite surface (green shades), (ii) an α-$Al_2O_3(0001)$ slab (blue shades), and (iii) a graphene-coated α-$Al_2O_3(0001)$ slab (orange shades). Bold colours indicate single-collision events, whereas lighter shades denote multiple-collision trajectories that ultimately escape from the surface.

Alt text: Bar chart showing the collision statistics for nitrogen scattering trajectories on three different surfaces: graphite, alumina, and graphene-coated alumina at different impingement angles (30, 45, and 70 degrees). For each surface, the bars are divided into two categories: single-collision events and multiple-collision events. The chart indicates that for all three surfaces and all impingement angles, the majority of trajectories are single-collision events. An exception is the case of graphene-coated alumina at 70 degrees, where multiple-collision events are more prevalent.

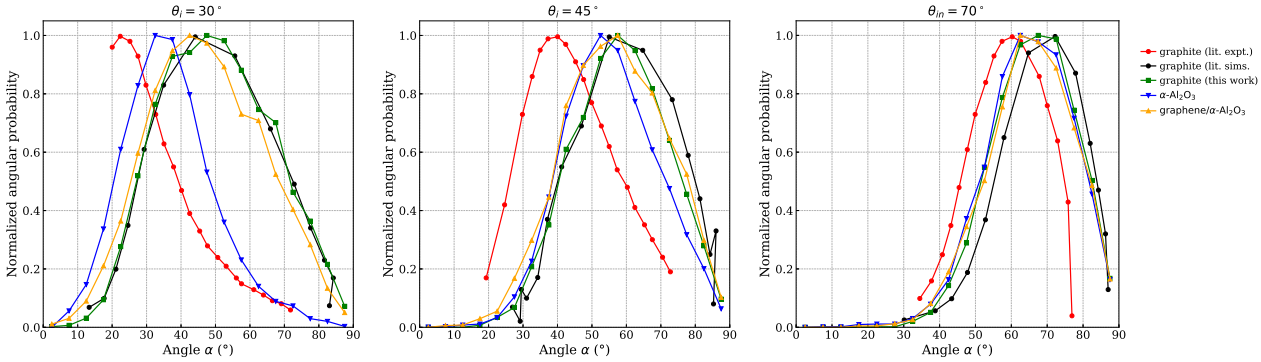

FIG. S6. Cartesian plot version of Fig. 2 in the main text.

Alt text: Angular distribution of reflected trajectories for nitrogen scattering on three different surfaces: graphite, alumina, and graphene-coated alumina at different impingement angles (30, 45, and 70 degrees) compared with teoretical and experimental data from litterature. It represents a Cartesian plot of the polar plot shown in Fig. 2 in the main text.

corresponding distribution of reflected velocities (see Figs. S7 and S8). We then fit a straight line to the collision data using a least-squares procedure (red line). The slope of this fit corresponds to the fractional term in Eq. (2) of the main text; by comparing it with the horizontal dashed line (fully diffusive limit) and the diagonal dashed line (fully specular limit), we extract the accommodation coefficient.

S7. PROPORTION OF SPECULAR VS. DIFFUSIVE SCATTERING

Fig. S9 reports the fraction of reflected trajectories as a function of defects concentration in graphene coated alumina for vacancies, divacancies, and Stone-Wales defects in the TAC calculations. Unlike the gas-beam simulations—where the incident angle and kinetic energy are fixed—the TAC framework samples molecules impinging with a broad range of orientations and energies. Consequently, a finite fraction of low-energy molecules becomes trapped at the surface, which is unavoidable even when using long maximum propagation times (100 ps).

For pristine graphene, as well as for vacancy, divacancy and Stone-Wales defects, we observe comparable reflected fractions,

indicating that surface corrugation is not the dominant factor underlying the TAC increase in these cases.

S8. CORRUGATION SENSITIVE ANALYSIS

Figure S10 shows the CAF as function of defect concentration for; vacancies, divacancies and Stone-Wales varying the interface well depth of alumina-graphene interactions by $\pm 10\%$. We note that CAF is virtually unchanged, due the week absorption of graphene on alumina surface, in agreement with Ref.[12].

S9. STRAINED GRAPHENE ON ALUMINA AND CORRUGATION

Different lattice parameters are chosen to impose controlled strain on pristine graphene supported on the alumina surface. Figure S11 shows the corrugation amplification factor (CAF) for strained pristine graphene on alumina. As expected, the CAF increases with increasing compressive strain[24]. In particular, pristine graphene under 2% compressive strain exhibits a CAF of 5.1, which is larger than the maximum value obtained for the defective graphene cases (Stone–Wales), for which CAF = 3.63.

We therefore select pristine graphene at 2% compressive strain for the TAC calculations reported in Fig. 5b of the main text. Since this system contains no lattice defects, the results indicate that corrugation is a primary driver of the TAC enhancement. A similar effect can also be induced by defects, although to different extents: this is evident for vacancy and divacancy defects, which produce a comparatively smaller increase in corrugation.

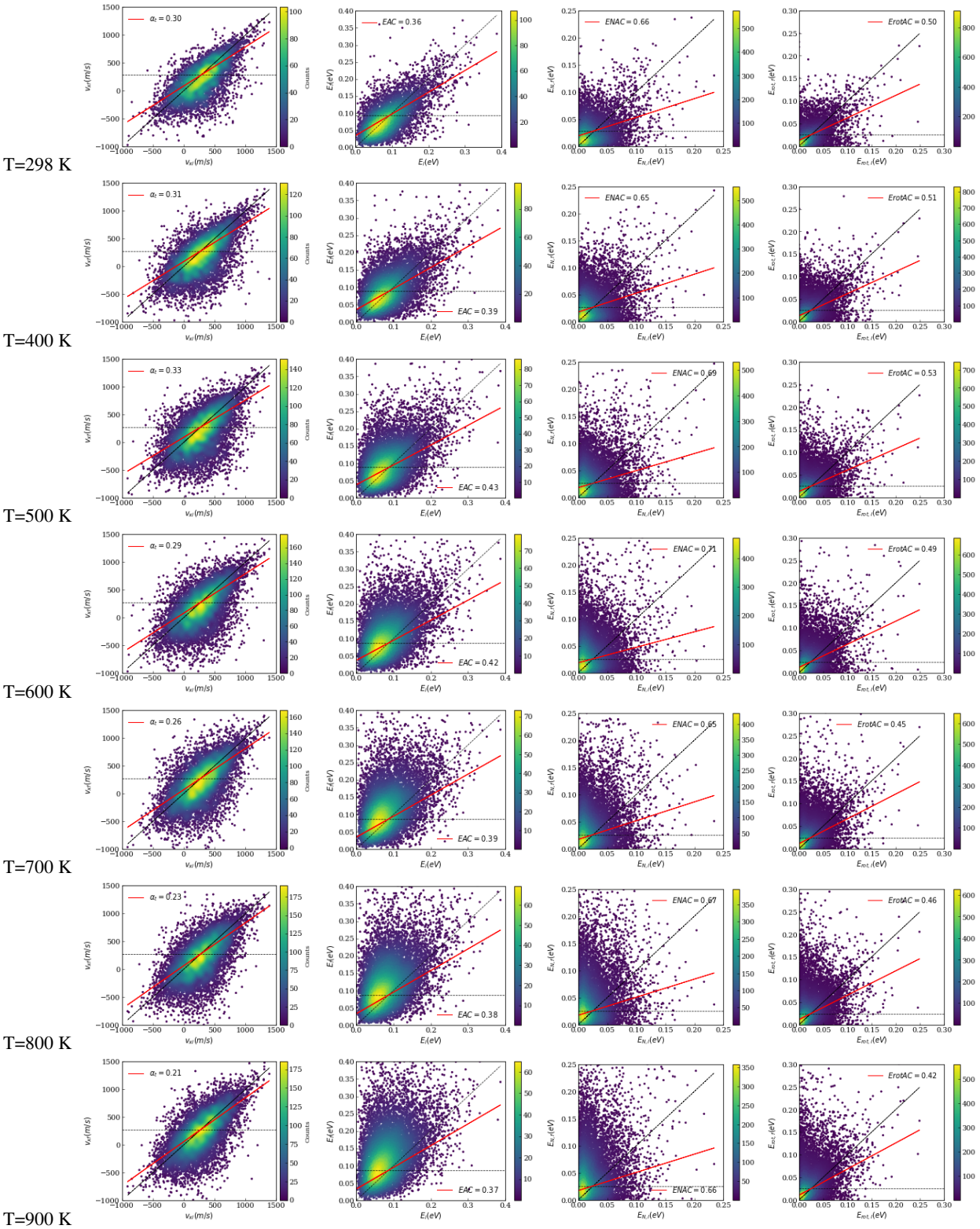

FIG. S7. TMAC, EAC, ENAC, and E_{rot}AC are obtained from the correlation between incident and reflected quantities for the alumina surface. The dashed horizontal and diagonal lines indicate the fully diffusive and fully specular limits, respectively. The red line denotes the least-squares linear fit to the collision data extracted from the MD simulations.

Alt text: The figure presents scatter plots with the fit for the accommodation coefficients (TMAC, EAC, ENAC, and E_{rot}AC) for the alumina surface as a function of temperature.

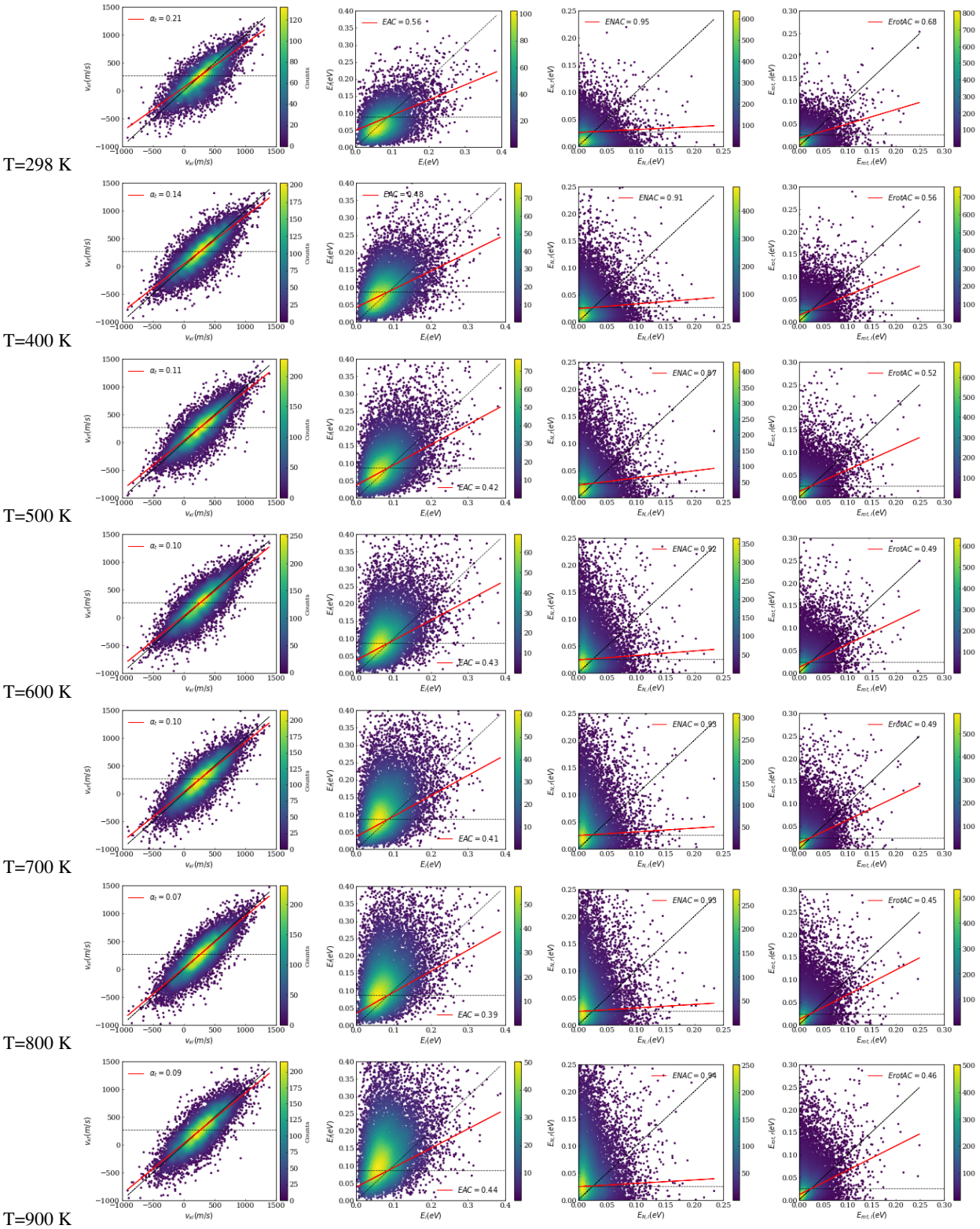

FIG. S8. TMAC, EAC, ENAC, and E_{rot}AC are obtained from the correlation between incident and reflected quantities for graphene-coated alumina. The dashed horizontal and diagonal lines indicate the fully diffusive and fully specular limits, respectively. The red line denotes the least-squares linear fit to the collision data extracted from the MD simulations.

Alt text: The figure presents scatter plots with the fit for the accommodation coefficients (TMAC, EAC, ENAC, and E_{rot}AC) for the graphene-coated alumina surface as a function of temperature.

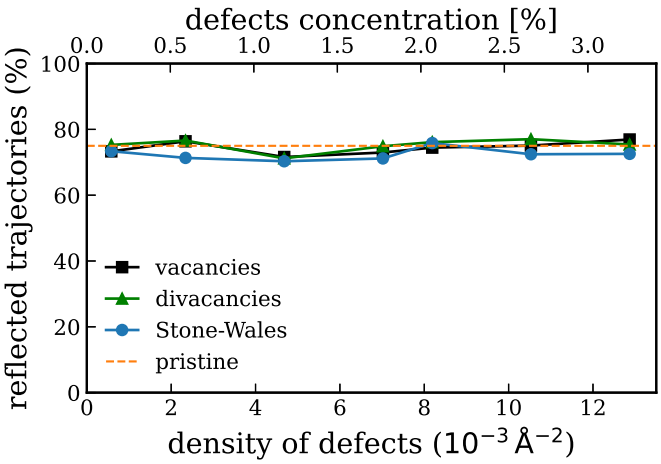

FIG. S9. Percentage of reflected trajectories as a function of defects concentration for vacancies (black circles), divacancies (green squares), and Stone-Wales defects (light-blue circles) in graphene. The orange dashed line indicates the pristine graphene reference.

Alt text: The plot shows the percentage of reflected trajectories as a function of defect concentration for pristine graphene and the three types of defects (vacancies, divacancies, and Stone-Wales) as a function of defect concentration. The percentage, close to 75% for all the cases, remains relatively constant across the range of defect concentrations.

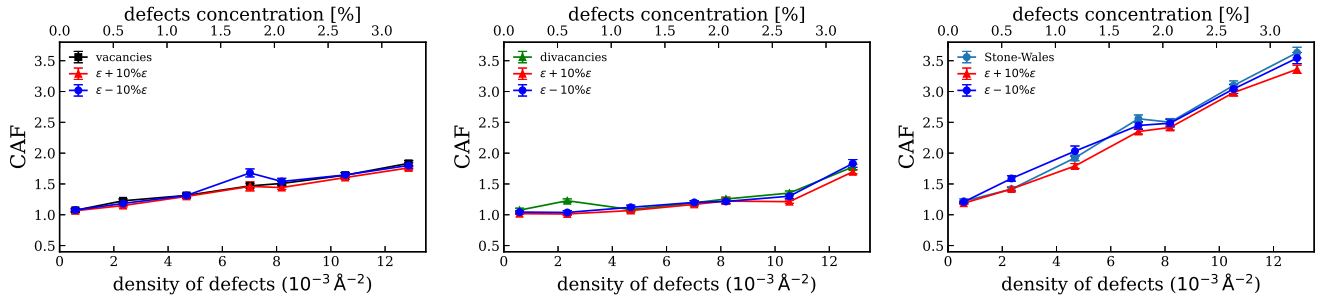

FIG. S10. Sensitivity analysis for CAF vs. defect concentration in the case of vacancies (left), divacancies (center) and Stone-Wales (right). The red and blue lines correspond to results obtained with a modified LJ potential where the well energy ε is respectively increased or decresed by 10%.

Alt text: The three panels show the corrugation amplification factor (CAF) as a function of defect concentration for vacancies, divacancies, and Stone -Wales defects, respectively. In each panel together with the curve obtained with the fitted LJ potential we also report the results obtained by modifying the LJ potential well depth ε by $\pm 10\%$. The results show that the CAF is almost insensitive to these modifications.

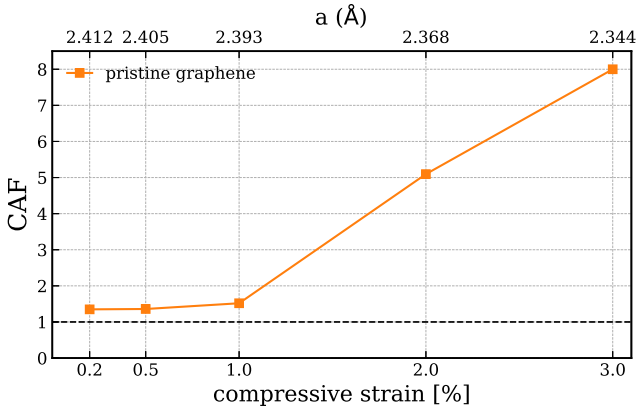

FIG. S11. CAF for compressed pristine graphene on alumina.

Alt text: The plot shows the corrugation amplification factor (CAF) for compressed pristine graphene on alumina as a function of strain. The CAF monotonically increases with increasing compressive strain, reaching a value of 8 at 3% compressive strain.

[1]P. Giannozzi, S. Baroni, N. Bonini, M. Calandra, R. Car, C. Cavazzoni, D. Ceresoli, G. L. Chiarotti, M. Cococcioni, I. Dabo, A. Dal Corso, S. de Gironcoli, S. Fabris, G. Fratesi, R. Gebauer, U. Gerstmann, C. Gougoussis, A. Kokalj, M. Lazzeri, L. Martin-Samos, N. Marzari, F. Mauri, R. Mazzarello, S. Paolini, A. Pasquarello, L. Paulatto, C. Sbraccia, S. Scandolo, G. Sclauzero, A. P. Seitsonen, A. Smogunov, P. Umari, and R. M. Wentzcovitch, "QUANTUM ESPRESSO: a modular and open-source software project for quantum simulations of materials," J. Phys.: Condens. Matter **21**, 395502 (2009).
[2]P. Giannozzi, O. Andreussi, T. Brumme, O. Bunau, M. Buongiorno Nardelli, M. Calandra, R. Car, C. Cavazzoni, D. Ceresoli, M. Cococcioni, N. Colonna, I. Carnimeo, A. Dal Corso, S. de Gironcoli, P. Delugas, R. A. DiStasio, A. Ferretti, A. Floris, G. Fratesi, G. Fugallo, R. Gebauer, U. Gerstmann, F. Giustino, T. Gorni, J. Jia, M. Kawamura, H.-Y. Ko, A. Kokalj, E. Küçükbenli, M. Lazzeri, M. Marsili, N. Marzari, F. Mauri, N. L. Nguyen, H.-V. Nguyen, A. Otero-de-la Roza, L. Paulatto, S. Poncé, D. Rocca, R. Sabatini, B. Santra, M. Schlipf, A. P. Seitsonen, A. Smogunov, I. Timrov, T. Thonhauser, P. Umari, N. Vast, X. Wu, and S. Baroni, "Advanced capabilities for materials modelling with Quantum ESPRESSO," J. Phys.: Condens. Matter **29**, 465901 (2017).
[3]P. Giannozzi, O. Baseggio, P. Bonfà, D. Brunato, R. Car, I. Carnimeo, C. Cavazzoni, S. de Gironcoli, P. Delugas, F. Ferrari Ruffino, A. Ferretti, N. Marzari, I. Timrov, A. Urru, and S. Baroni, "Quantum ESPRESSO toward the exascale," J. Chem. Phys. **152**, 154105 (2020).
[4]G. Prandini, A. Marrazzo, I. E. Castelli, N. Mounet, and N. Marzari, "Precision and efficiency in solid-state pseudopotential calculations," npj Computational Materials **4** (2018), 10.1038/s41524-018-0127-2.
[5]D. Vanderbilt, "Soft self-consistent pseudopotentials in a generalized eigenvalue formalism," Phys. Rev. B **41**, 7892–7895 (1990).
[6]E. Kucukbenli, M. Monni, B. I. Adetunji, X. Ge, G. A. Adebayo, N. Marzari, S. de Gironcoli, and A. D. Corso, "Projector augmented-wave and all-electron calculations across the periodic table: a comparison of structural and energetic properties," (2014), arXiv:1404.3015 [cond-mat.mtrl-sci].
[7]A. Dal Corso, "Pseudopotentials periodic table: From H to Pu," Computational Materials Science **95**, 337–350 (2014).
[8]J. P. Perdew, K. Burke, and M. Ernzerhof, "Generalized Gradient Approximation Made Simple," Phys. Rev. Lett. **77**, 3865–3868 (1996).
[9]S. Grimme, J. Antony, S. Ehrlich, and H. Krieg, "A consistent and accurate ab initio parametrization of density functional dispersion correction (dft-d) for the 94 elements h-pu," The Journal of Chemical Physics **132**, 154104 (2010).
[10]J. I. Hütner, A. Conti, D. Kugler, F. Mittendorfer, G. Kresse, M. Schmid, U. Diebold, and J. Balajka, "Stoichiometric reconstruction of the Al_2O_3 (0001) surface," Science **385**, 1241–1244 (2024).
[11]A. Marmier and S. C. Parker, "Ab initio morphology and surface thermodynamics of $\alpha - Al_2O_3$," Phys. Rev. B **69**, 115409 (2004).
[12]D. Acharya, D. Perilli, and C. Di Valentin, "Optimizing the graphene/$\alpha - Al_2O_3$(0001) interface through minimization of interfacial stress for improved electronic applications," ACS Appl. Nano Mater. **8**, 22626–22636 (2025).
[13]S. Ou, J. E. Heimann, and J. W. Bennett, "A Density Functional Theory (DFT) Investigation of Sulfur-Based Adsorbate Interactions on Alumina and Calcite Surfaces," Clays Clay Miner. **70**, 370–385 (2022).
[14]B. Ramogayana, D. Santos-Carballal, K. P. Maenetja, N. H. de Leeuw, and P. E. Ngoepe, "Density Functional Theory Study of Ethylene Carbonate Adsorption on the (0001) Surface of Aluminum Oxide α-Al_2O_3," ACS Omega **6**, 29577–29587 (2021).
[15]A. Biaggne, G. Noble, and L. Li, "Adsorption and Surface Diffusion of Metals on α-Al_2O_3 for Advanced Manufacturing Applications," JOM **73**, 1062–1070 (2021).
[16]R. Storn and K. Price, "Differential evolution – a simple and efficient heuristic for global optimization over continuous spaces," J. Glob. Optim. **11**, 341–359 (1997).
[17]P. Lazić, "Cellmatch: Combining two unit cells into a common supercell with minimal strain," Comput. Phys. Commun. **197**, 324–334 (2015).
[18]P. Vashishta, R. K. Kalia, A. Nakano, and J. P. Rino, "Interaction potentials for alumina and molecular dynamics simulations of amorphous and liquid alumina," J. Appl. Phys. **103**, 083504 (2008).
[19]S. J. Stuart, A. B. Tutein, and J. A. Harrison, "A reactive potential for hydrocarbons with intermolecular interactions," J. Chem. Phys. **112**, 6472–6486 (2000).
[20]J. Beránek, A. Böhm, G. Palermo, J. Martinovič, and B. Jansík, "Hyperqueue: Efficient and ergonomic task graphs on hpc clusters," SoftwareX **27**, 101814 (2024).
[21]N. A. Mehta, D. A. Levin, V. J. Murray, and T. K. Minton, "Study of non-reactive scattering from graphene using molecular beam experiments and molecular dynamics," AIP Conf. Proc. **1786**, 100003 (2016).
[22]S. Cajahuaringa, D. L. Z. Caetano, L. N. Zanotto, G. Araujo, and M. S. Skaf, "Massccs: A high-performance collision cross-section software for large macromolecular assemblies," J. Chem. Inf. Model **63**, 3557–3566 (2023).
[23]P. Spijker, A. J. Markvoort, P. A. J. Hilbers, S. V. Nedea, and T. Abe, "Velocity correlations and accommodation coefficients for gas-wall interactions in nanochannels," in *AIP Conf. Proc.* (AIP, 2008) pp. 659–664.
[24]F. L. Thiemann, P. Rowe, A. Zen, E. A. Müller, and A. Michaelides, "Defect-dependent corrugation in graphene," Nano Lett. **21**, 8143–8150 (2021).